# CHAPTER 2

## A Planar Shaped-Beam Antenna with metal grating

2-1. STRUCTURE CONFIGURATION

As shown in figure 1(a), the antenna under consideration contains an air separator with thickness denoted as d_1, sandwiched between a metal plate and metal strips array (metal grating) coated on a dielectric substrate. The width, length and thickness of each metal strip are a, l and t_m, respectively. The period of the metal strip array is b. The dielectric layer has the thickness t_d and relative dielectric constant ε_r. The structure is excited by a line source made up of a coaxial probe. The distance from the line source to the metal plate is d_2. The width of the antenna is $(N-1)b+a$, where N is the number of periods along the x direction. To have a symmetric radiation pattern in the forward direction, the line source is placed at the center along the x direction.
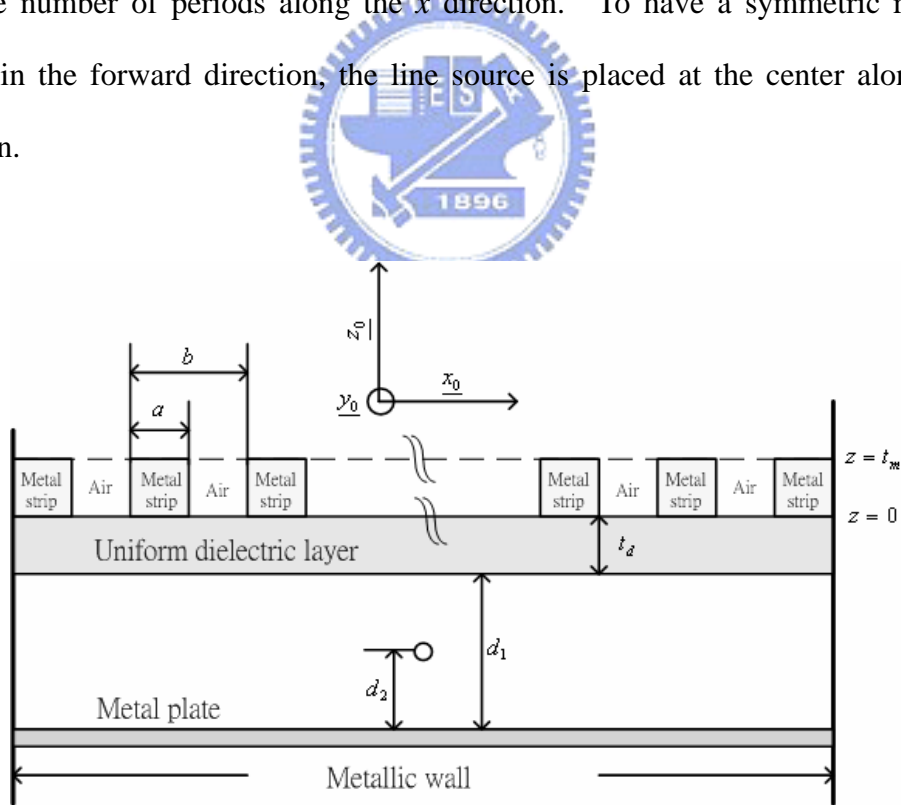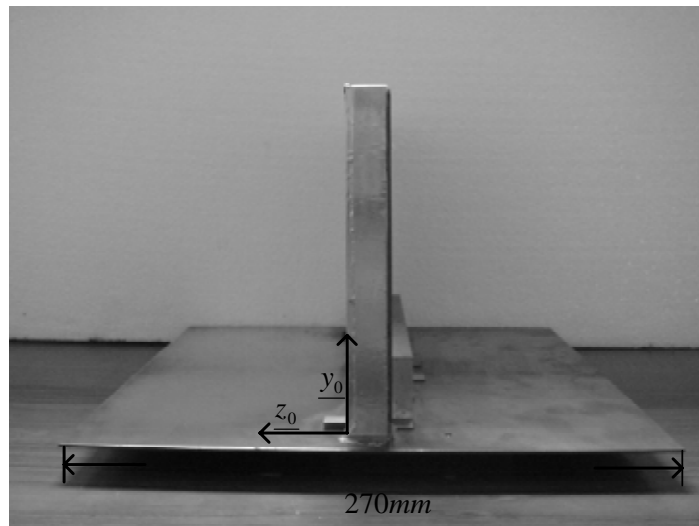

(a)
Figure 1: The planar shaped-beam antenna; (a) structure configuration and parameters assignment
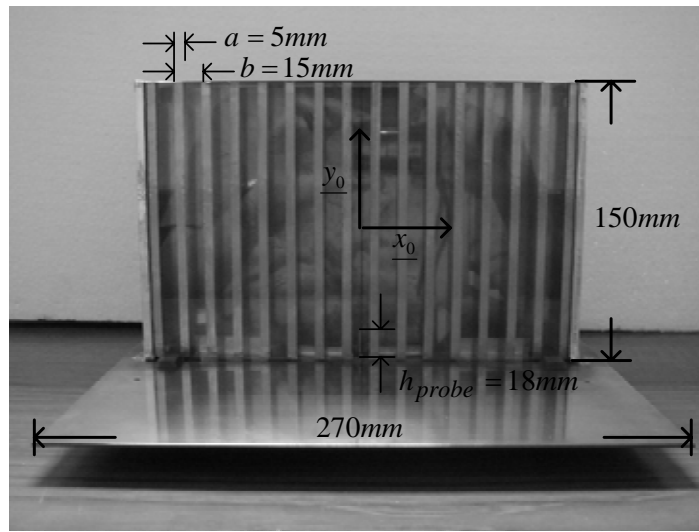
(b)

(c)

Figure 1: The planar shaped-beam antenna; (b) front view, and (c) side view

2-2. METHOD OF ANALYSIS

For the theoretical formulation, since the length of the structure along the y-direction is greater than five times of the operation wavelength, the structure is assumed to have no electromagnetic fields variation along the y the direction. Accordingly, the electromagnetic field problem could be regarded as a two-dimensionally boundary-value problem. The individual polarization (E_y mode) is considered only, without dealing with the cross-polarization problem. Returning to figure 1(a), since the structure has only one open end along the +z direction, the radiation far-field can be approximately calculated by the equivalent sources, including the electric- and magnetic- source, induced on the outmost surface of the metal grating. To resolve the electromagnetic fields on the outer surface of metal grating, we have to solve the electromagnetic fields in the parallel-plate waveguide (PPWG) consisting of multiple junction discontinuities. Because that the structure consists of many typical PPWGs whose mode functions are well known (the unknown to be determined are the modal amplitudes), the mode-matching method was employed to formulate the electromagnetic boundary-value problem. The electric field is assumed to be vanished in the metal strip (perfect electric conductor), thus, the region between two adjacent metal strips can be regarded as a sub-PPWG. Consequently, the electromagnetic fields are expressed in term of the summation of PPWG modes. By matching the tangential electric and magnetic fields across the discontinuities between the sub-PPWGs and the oversized PPWG, the original electromagnetic fields problem can be converted into the cascades of transmission line networks including an excitation current source. Therefore, the modal voltage and current everywhere are determined by solving the transmission-line network.

The representation of the electric and magnetic fields within a uniform waveguide can be reformulated into an engineering description in terms of an infinite number of

modal voltages and currents. The variation of each modal voltage and current along the guide axis is described in terms of the corresponding variation of voltage and current along an appropriate transmission line. The description of the entire field within the guide is thereby reduced to the description of the electrical behavior on an infinite set of transmission lines.

Since the mathematical procedure of mode-matching method was well known in microwave engineering, we listed some important equations while the detail mathematical procedures can be found in the appendix.

As mentioned earlier, the metal strip is assumed to have infinite conductivity; thus, the electric fields exist in the sub- and oversized- PPWG region. The electric and magnetic fields in the oversized-PPWG or sub-PPWGs can be expressed in terms of the superposition of PPWG modes, which are given below.

$$E_y(x,z) = -\sum_{n=1}^{\infty} \overline{V}_n^{(i)}(z)\overline{\phi}_n^{(i)}(x); \ x \in i-th \text{ aperture} \tag{2.1}$$

$$H_x(x,z) = \sum_{n=1}^{\infty} \overline{I}_n^{(i)}(z)\overline{\phi}_n^{(i)}(x); \ x \in i-th \text{ aperture} \tag{2.2}$$

with $\overline{\phi}_n^{(i)}(x) = \sqrt{\dfrac{2}{w_i}} \sin \dfrac{n\pi(x - x_i)}{w_i}, x \in [x_i, x_i + w_i]$ (2.3)

where x_i and w_i are the start position and width of the *i-th* aperture.

where the *V*'s and *I*'s denote the voltage and current waves in each parallel-plate waveguide, which satisfy the transmission line equations along the *z* direction given as follow

$$\frac{dV_n(z)}{dz} = -jk_{zn}Z_n I_n(z) \tag{2.4}$$

$$\frac{dI_n(z)}{dz} = -jk_{zn}Y_n V_n(z) \tag{2.5}$$

Where the k_{zn} and Z_n (Y_n) are the propagation constant and impedance (admittance) along the z-direction, which are written as

$$k_{zn} = \sqrt{k_o^2 \varepsilon_r - (n\pi / s)^2} \tag{2.6}$$

$$Z_n = \omega\mu_o / k_{zn} \tag{2.7}$$

After matching the tangential electric and magnetic fields at the discontinuity ($z = t_m$) across the uniform layer and metal grating, the voltage and current waves in respective regions are related by the following equations.

$$V_m(t_m^+) = \sum_{i=1}^{N}\sum_{n=1}^{\infty} \left\langle \phi_m(x) \middle| \overline{\phi}_n^{(i)}(x) \right\rangle \overline{V}_n^{(i)}(t_m^-) \tag{2.8}$$

$$\overline{I}_m^{(i)}(t_m^-) = \sum_{n=1}^{\infty} \left\langle \phi_n(x) \middle| \overline{\phi}_m^{(i)}(x) \right\rangle I_n(t_m^+) \tag{2.9}$$

$$\overline{V}_m^{(i)}(t_m^-) = \sum_{n=1}^{\infty} \left\langle \phi_n(x) \middle| \overline{\phi}_m^{(i)}(x) \right\rangle V_n(t_m^+) \tag{2.10}$$

with the notation $\left\langle \phi_m(x) \middle| \overline{\phi}_n^{(i)}(x) \right\rangle = \int_{x_i}^{x_i+w_i} \phi_m(x)\overline{\phi}_n^{(i)}(x)dx$ (2.11)

Where the parameter i denotes the index number of the i-th aperture in the metal grating and the parameter N is the number of apertures. The parameters V's and I's are the modal- voltage and current amplitudes in the oversized waveguide, and $\phi(x)$ is the modal function along the x direction. The equations (2.8-10) define the relations of the modal- voltage and current between the oversized- and sub- PPWGs. By applying the same procedure at the interface $z = 0$, we could obtain the similar input-output relation for the modal- voltage and current.

The next step to be dealt with is the excitation problem. The line source embedded in the air separating layer can also be expressed in terms of the superposition of PPWG modes, each of which is viewed as the incident mode for the scattering

analysis. The modal voltage waves at the position of line source relate to the excitation current amplitude and the input impedance of each PPWG mode looking upward and downward from the position of excitation (see equation A17). Furthermore, the transmitted voltage (and current) waves of each waveguide mode from the position of excitation source to the outmost surface of the metal grating is determined by cascading the input-output relation derived previously. After taking the superposition for these transmitted voltage and current waves contributed by respective incident waveguide mode, the overall electric and magnetic fields distribution on the outmost surface of the antenna are obtained. Since this structure has only one open end, the backward and sideward radiations shall be negligible. The radiation far-field in the forward direction is determined using the two-dimensional Fourier transform of the aperture field on the outer surface of the metal grating. The equivalent- electric and magnetic currents on the outer surface are given as follows.

$$M_x(x) = -\sum_{n=1}^{\infty} V_n^{(s)}(t_m^+)\phi_n(x) \tag{2.12}$$

$$J_y(x) = \sum_{n=1}^{\infty} I_n^{(s)}(t_m^+)\phi_n(x) \tag{2.13}$$

where V's and I's in (12) and (13) represent the voltage and current waves of each PPWG mode of the oversized PPWG on the outmost surface. Notice that, in this research, we assumed that the electromagnetic fields have no variation along the y direction. Therefore, in the far-field radiation calculation, the equivalent sources were supposed to be uniform along the length of the radiating aperture, while the electric and magnetic fields are assumed to be vanished outside the radiation aperture.

2.3. NUMERICAL AND EXPERIMENTAL RESULTS

2.3.1 Measurement results of antenna

Figure 2 depicts the radiation pattern of the shaped-beam antenna developed in this paper.   This planar antenna was fabricated by printing the copper foil, with thickness 0.05 mm, on a dielectric substrate (acrylic) with thickness 1.86 mm and relative dielectric constant $\varepsilon r = 2.59$.   The excitation probe was placed between the metal grating and the metal plate, where the distance to the metal plate is 3 mm.   The width, length and period of the metal strip are 5 mm 150 mm and 15 mm, respectively.   The number of metal strips is 16.   The radiation pattern was measured in an anechoic chamber using vector network analyzer HP 8722D and broadband standard-gain horn antenna.

As we have known, the translation of power illumination pattern function with smooth continuous transitions (equation 9, [5]) to the far field in polar coordinates yields the $\sec^2$ pattern.   From figure 2(a) to 2(k), we demonstrated the measured, calculated and target ($\sec^2$) patterns for the cases with frequencies from 10.90 GHz, to 11.90 GHz, respectively.   The frequencies from 10.90 GHz to 11.90 GHz have the similar pattern shown in these figures.   It is apparently to see that the difference between target and measured patterns, in average, is within 1.5 dB.   The maximum coverage angle of equal radiated power along a straight line is about 90 degree.   Outside this range, the radiation power drastically falls off.   It is noted that this antenna radiates a $\sec^2$ pattern with vertical polarization in the azimuthal direction only.   It is very different with the present applications [5-7] having circular footprint and circular polarization.

From the radiation pattern, we may conjecture that the radiation mechanism is due to the leaky-wave phenomenon of the 1D metal grating [8].   The wave excited by the line source is propagating along the $\pm x$ direction, and is gradually decaying during their propagation.   As shown in figure 2, the power leaks away from the structure,

becoming leaky waves with two radiation peaks in the broadside direction.   However,

due to the incomplete power leakage and the existence of metal side walls, the

remaining power experiences multiple reflections and results in fluctuation in its

radiation pattern.   The curves shown in figure 2(a) to (k) could be used to predict

the area of uniform coverage.   If an imaginary plane was placed at a distance h from

the antenna, the uniform coverage length along the x axis is $L_{max}=h(cot\phi_1+ cot\phi_2)$

Where ϕ_1 and ϕ_2 are the lower and upper bounds of the azimuthal angle (in degree)

satisfying the condition of uniform coverage, which could be read from figure 2.   For

example, if the distance h is 0.52m, the maximum uniform coverage along the x axis

will be about 1.2m for the case shown in figure 2(a) with $\phi_1 =50^{o}$ and $\phi_2 =130^{o}$,
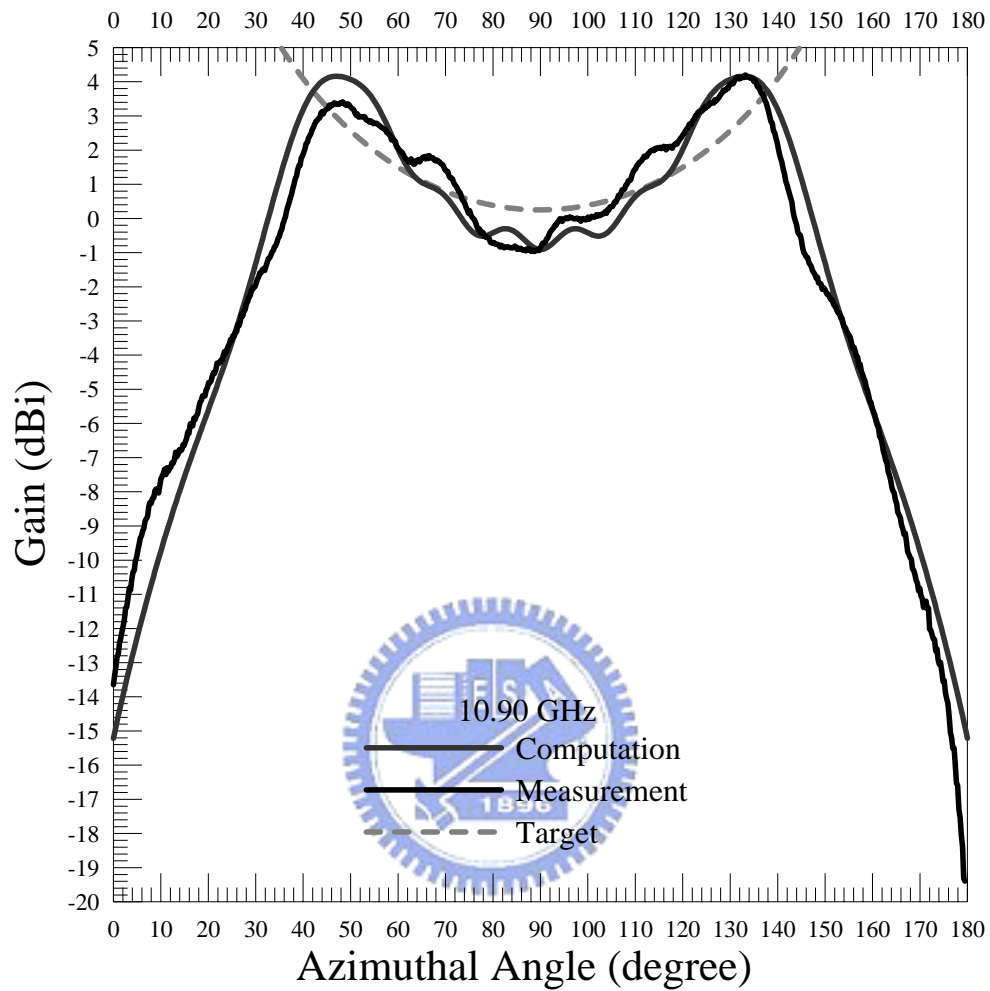
respectively.

Figure 2: Measured, computed and target patterns of the shaped-beam antenna (ε_r =2.59, a=5mm, b=15mm, t_m=0.05mm, t_d=1.86mm, d_1=12.52mm, d_2=3.0 mm, 16 metal strips); (a) 10.9GHz
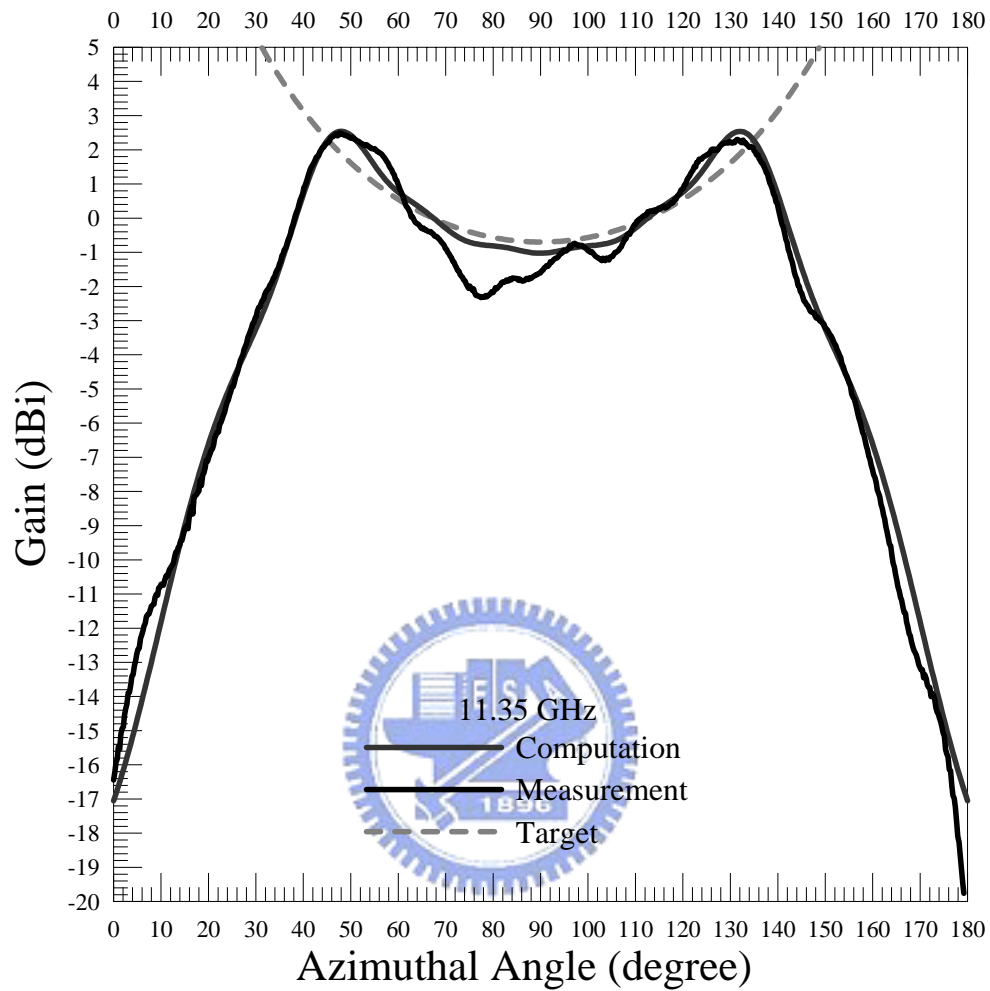
Figure 2: Measured, computed and target patterns of the shaped-beam antenna (ε_r=2.59, a=5mm, b=15mm, t_m=0.05mm, t_d=1.86mm, d_1=12.52mm, d_2=3.0 mm, 16 metal strips); (b) 11.35GHz.
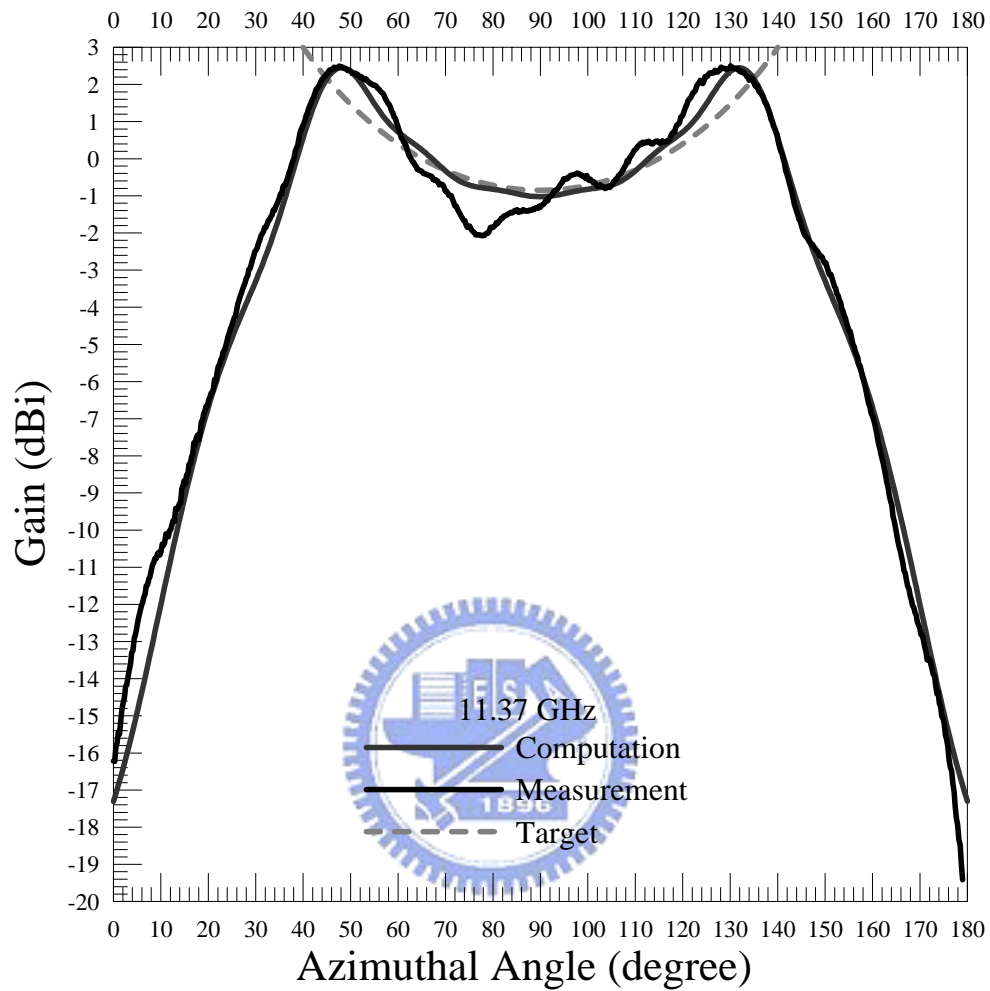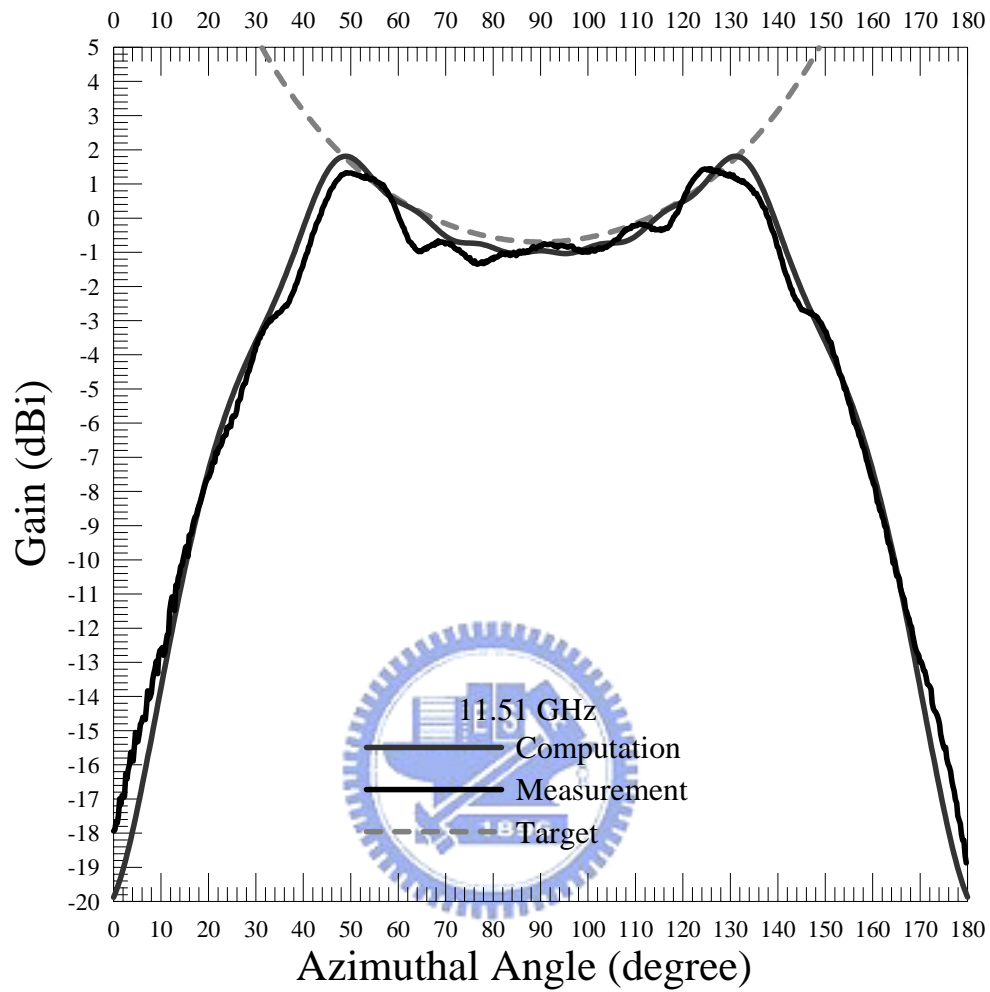
Figure 2: Measured, computed and target patterns of the shaped-beam antenna (ε_r=2.59, a=5mm, b=15mm, t_m=0.05mm, t_d=1.86mm, d_1=12.52mm, d_2=3.0 mm, 16 metal strips); (c) 11.37GHz.
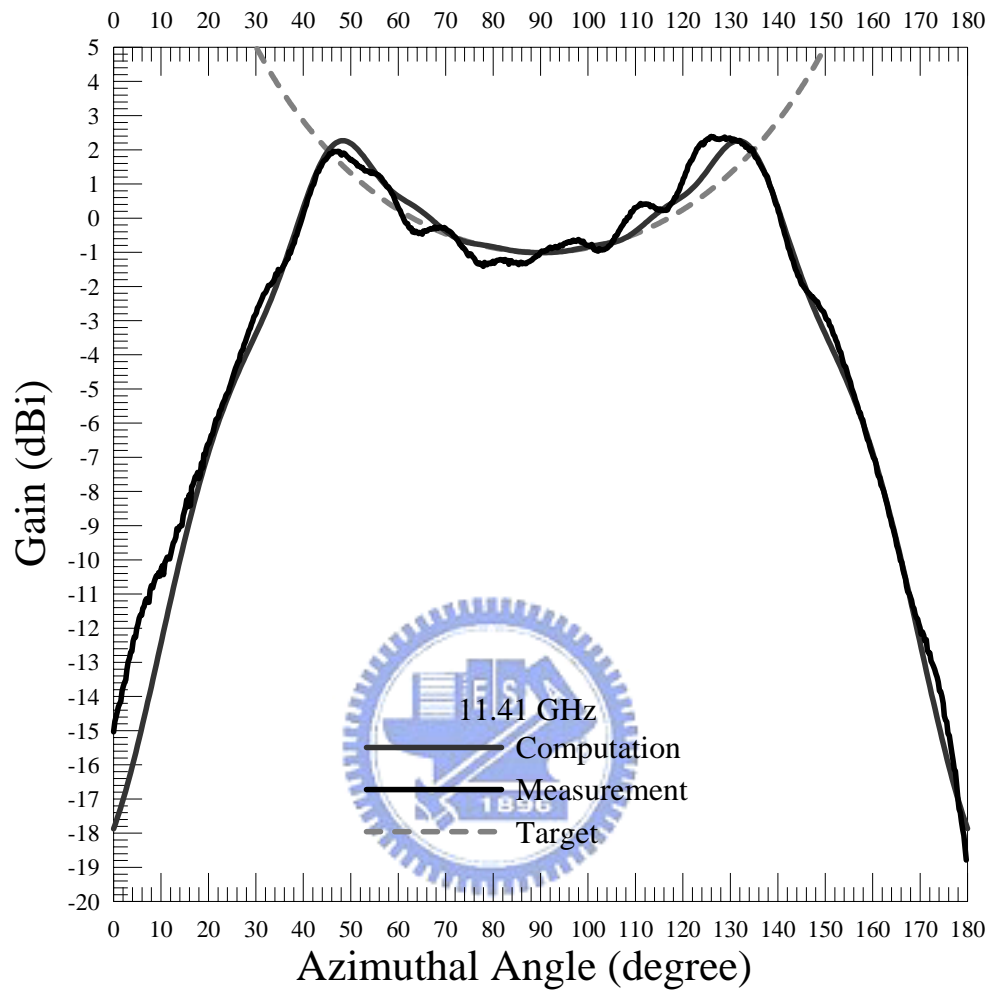
Figure 2: Measured, computed and target patterns of the shaped-beam antenna (ε_r=2.59, a=5mm, b=15mm, t_m=0.05mm, t_d=1.86mm, d_1=12.52mm, d_2=3.0 mm, 16 metal strips); (d) 11.41GHz.
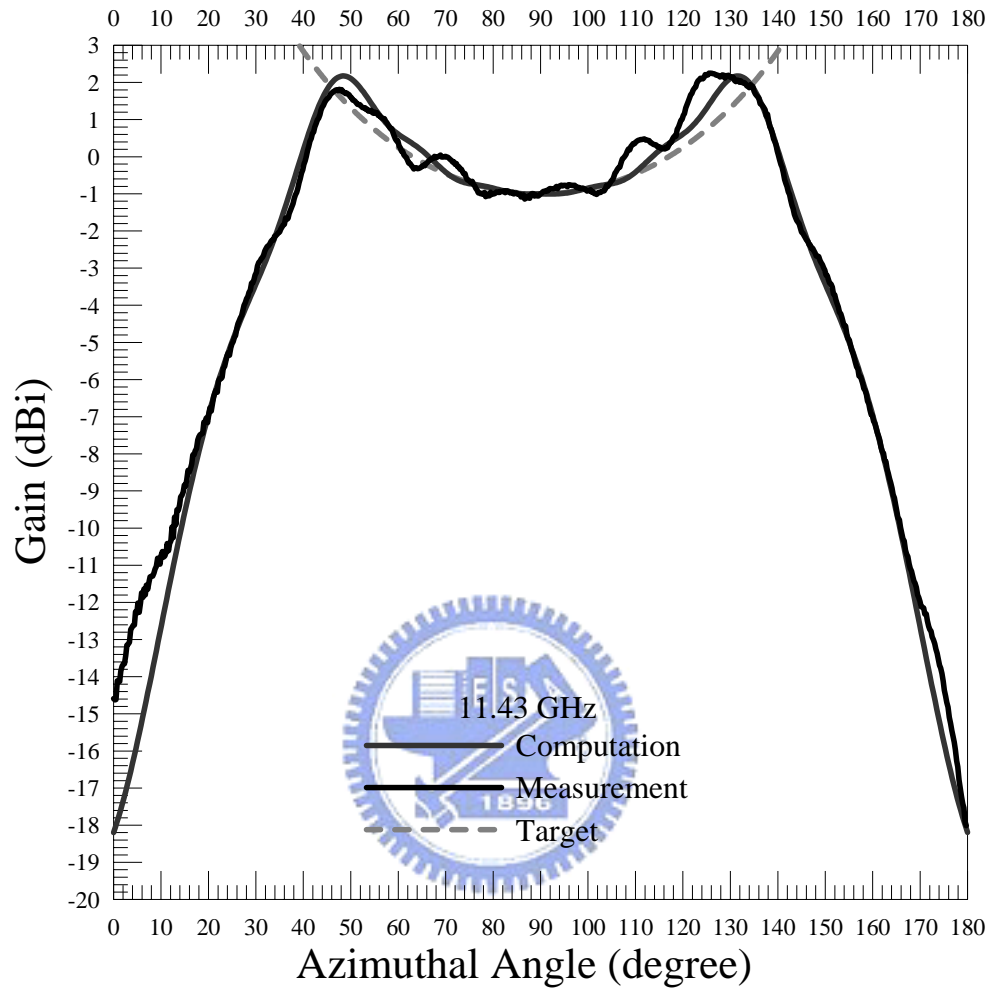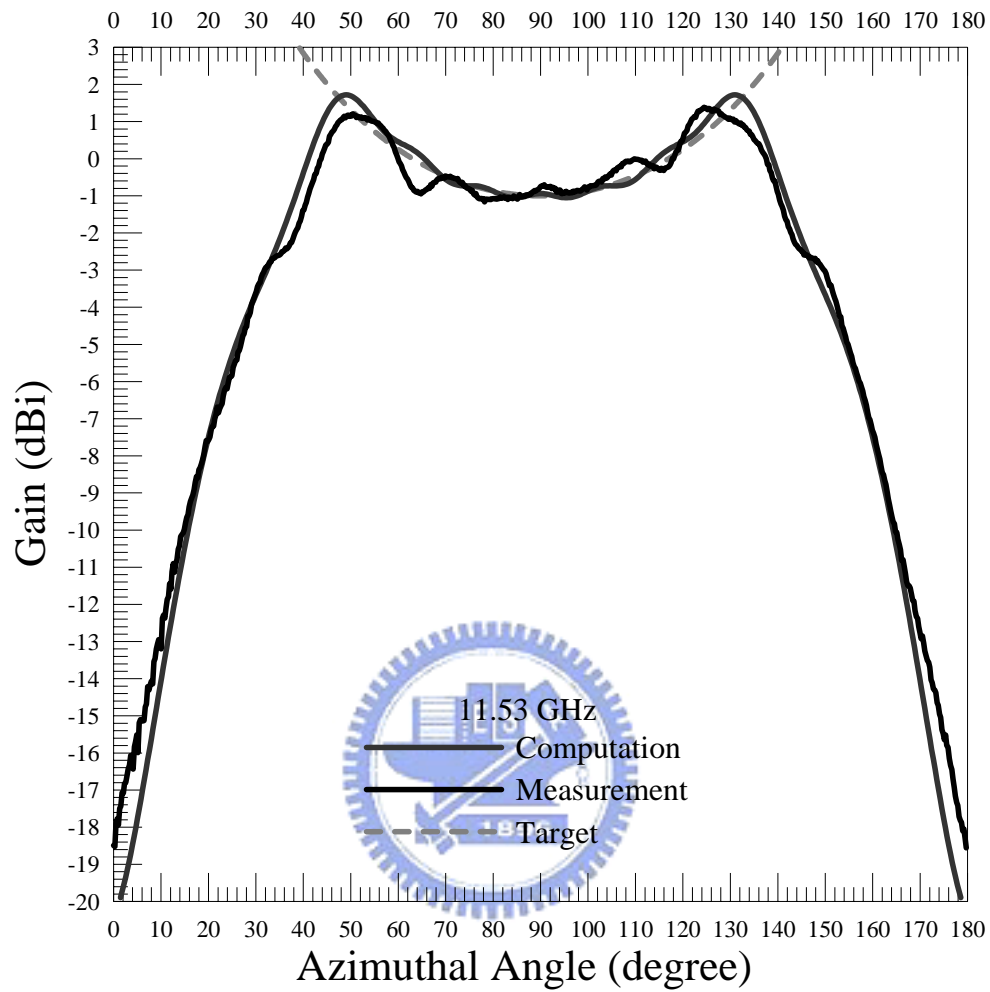
Figure 2: Measured, computed and target patterns of the shaped-beam antenna (ε_r =2.59, a=5mm, b=15mm, t_m=0.05mm, t_d=1.86mm, d_1=12.52mm, d_2=3.0 mm, 16 metal strips); (e) 11.43GHz.
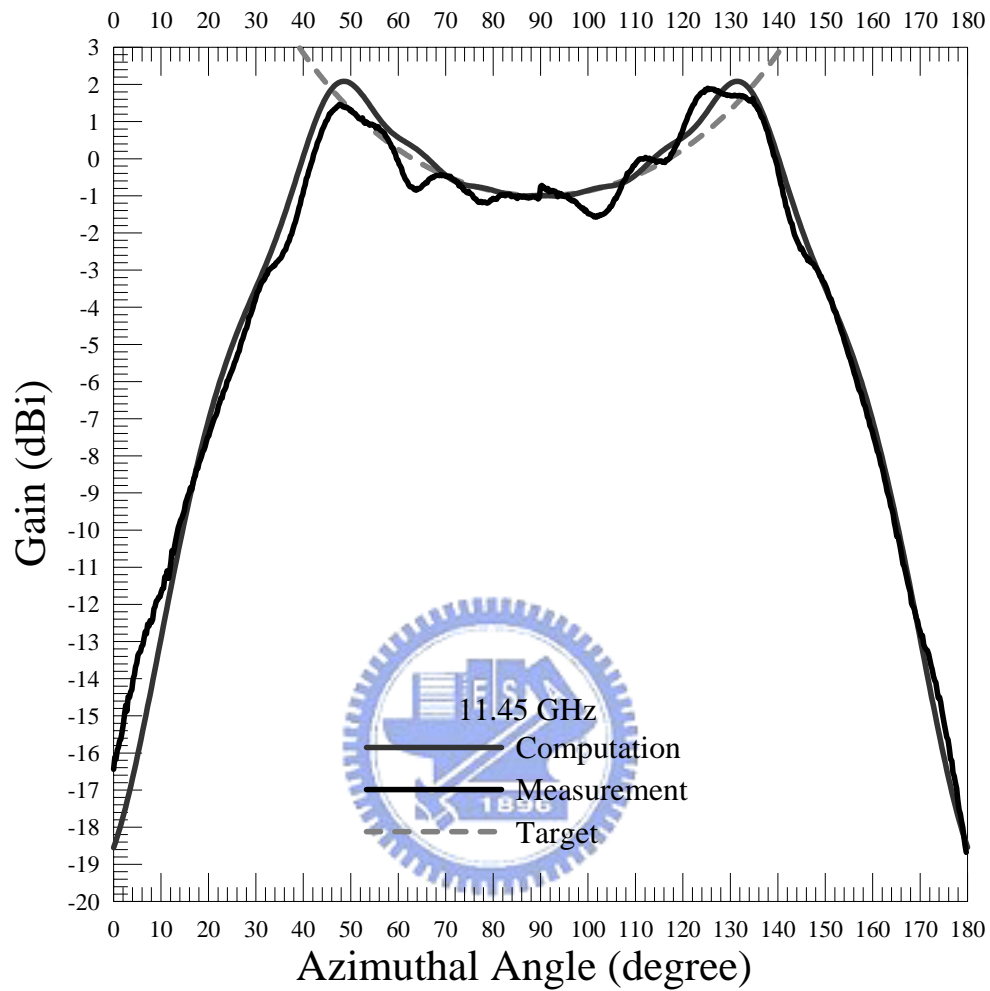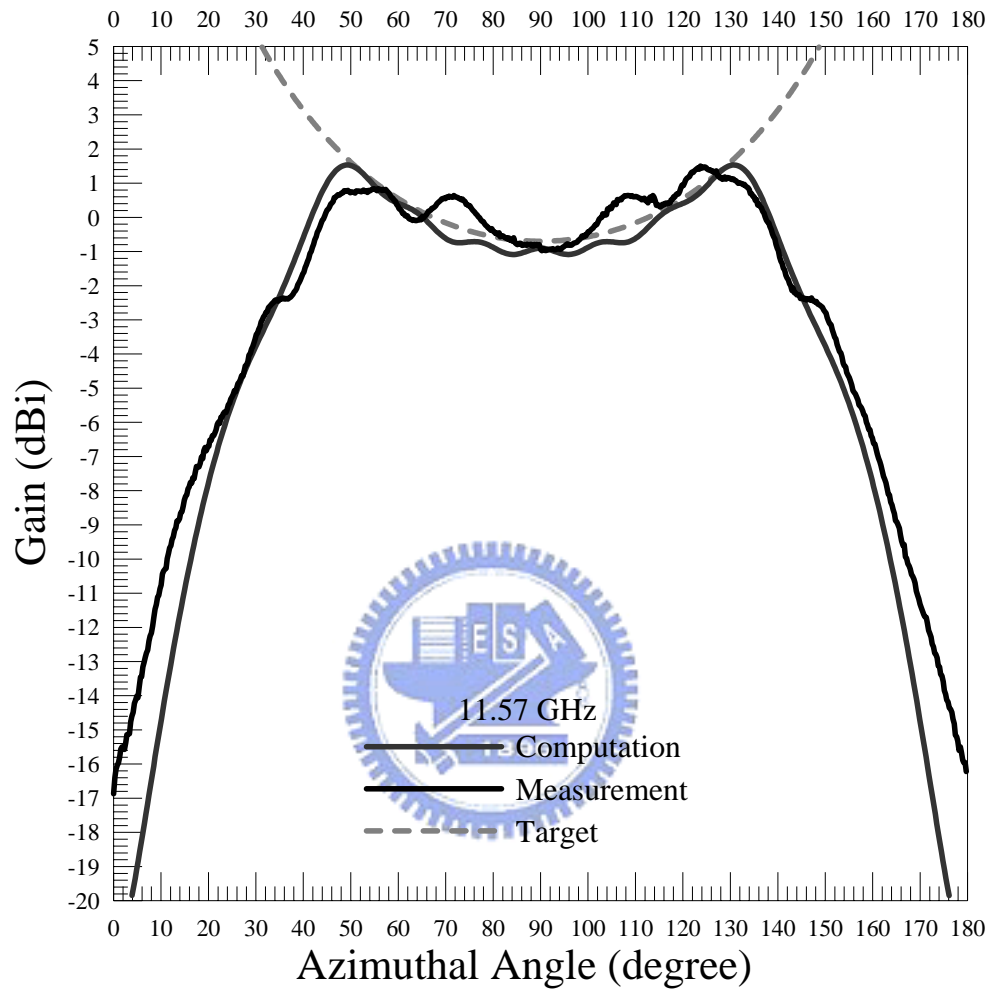
Figure 2: Measured, computed and target patterns of the shaped-beam antenna (ε_r =2.59, a=5mm, b=15mm, t_m=0.05mm, t_d=1.86mm, d_1=12.52mm, d_2=3.0 mm, 16 metal strips); (f) 11.45GHz.
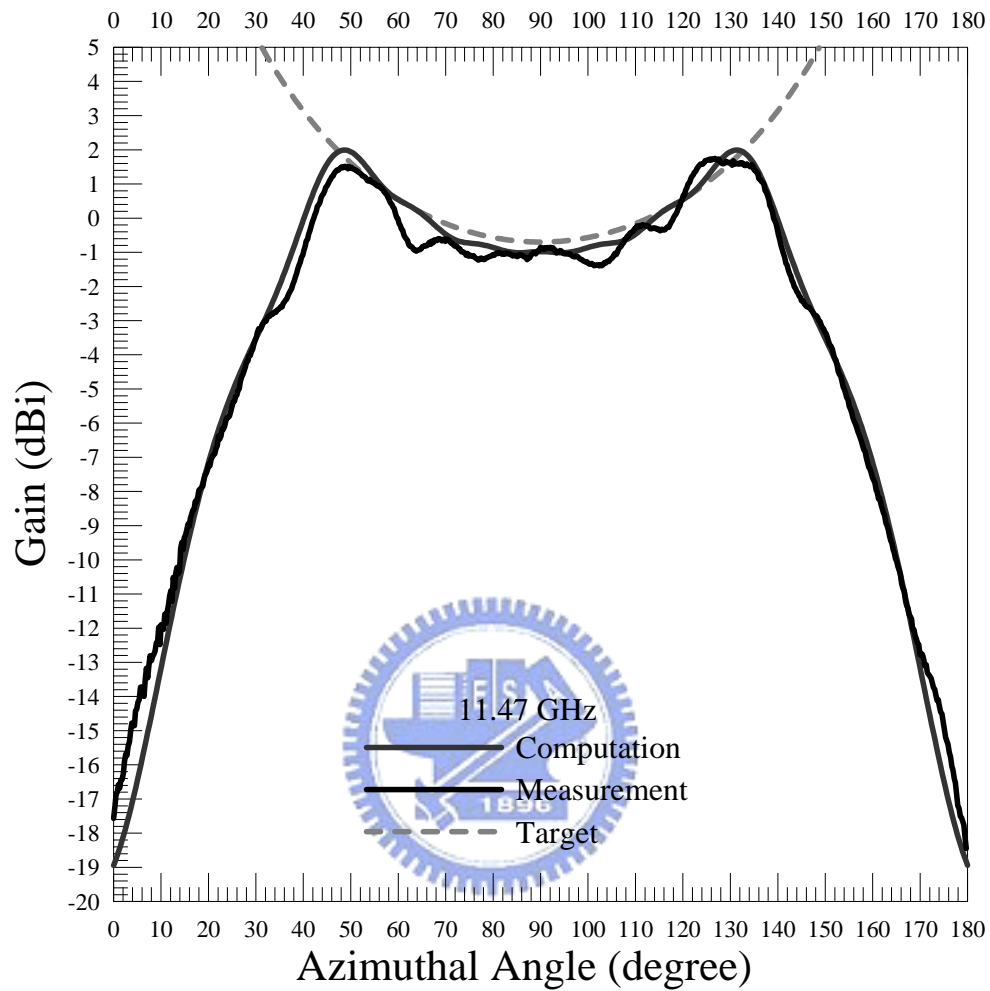
Figure 2: Measured, computed and target patterns of the shaped-beam antenna (ε_r=2.59, a=5mm, b=15mm, t_m=0.05mm, t_d=1.86mm, d_1=12.52mm, d_2=3.0 mm, 16 metal strips); (g) 11.47GHz.
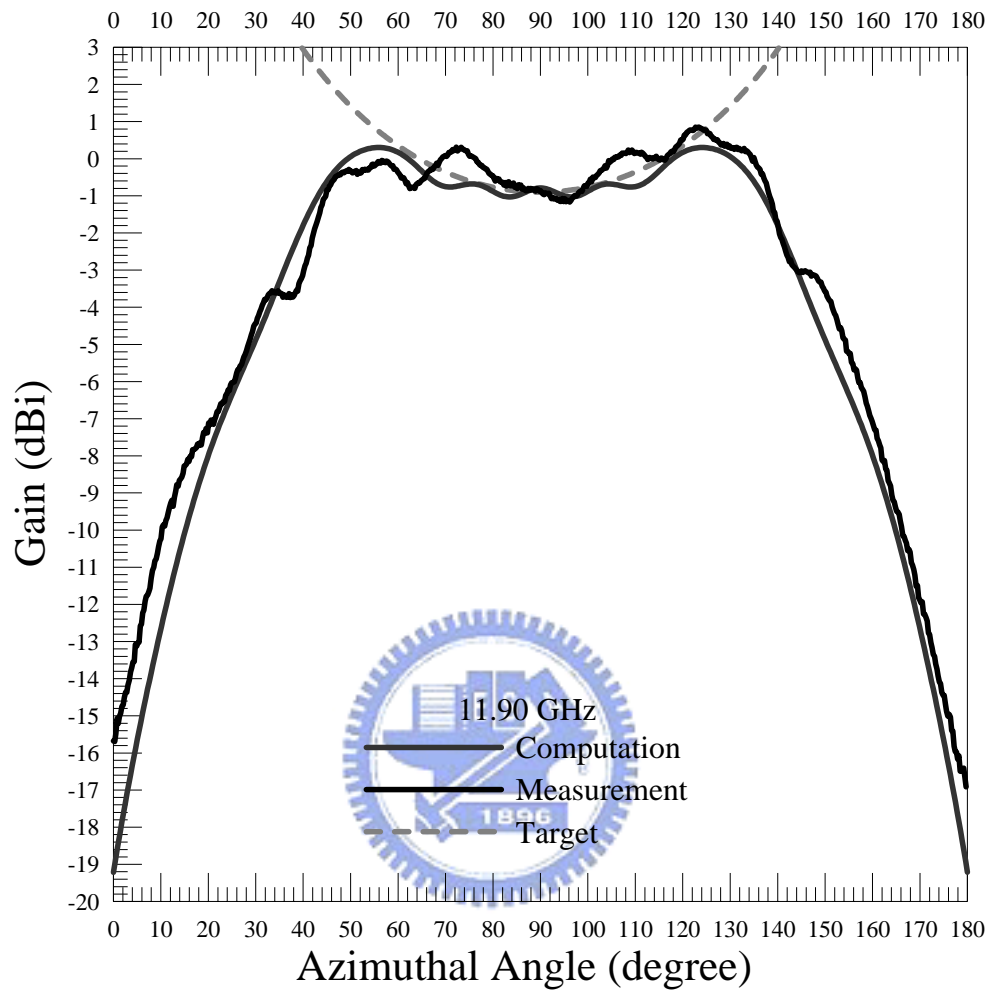
Figure 2: Measured, computed and target patterns of the shaped-beam antenna (ε_r =2.59, a=5mm, b=15mm, t_m=0.05mm, t_d=1.86mm, d_1=12.52mm, d_2=3.0 mm, 16 metal strips); (h) 11.51GHz.

Figure 2: Measured, computed and target patterns of the shaped-beam antenna (ε_r =2.59, a=5mm, b=15mm, t_m=0.05mm, t_d=1.86mm, d_1=12.52mm, d_2=3.0 mm, 16 metal strips); (i) 11.53GHz.

Figure 2: Measured, computed and target patterns of the shaped-beam antenna (ε_r=2.59, a=5mm, b=15mm, t_m=0.05mm, t_d=1.86mm, d_1=12.52mm, d_2=3.0 mm, 16 metal strips); (j) 11.57GHz.

Figure 2: Measured, computed and target patterns of the shaped-beam antenna (ε_r=2.59, a=5mm, b=15mm, t_m=0.05mm, t_d=1.86mm, d_1=12.52mm, d_2=3.0 mm, 16 metal strips); (k) 11.9GHz.

In the following example, we measured the y-direction electric-field strength on a rectangular plane in front of the antenna for the these cases with frequency 10.90 GHz, 11.37 GHz, 11.43GHz, 11.45GHz, 11.47GHz, 11.53GHz and 11.90 GHz, respectively. The measurement setup is shown in the attached figure 3 (a) to (c). The distance from the antenna to the rectangular plane is 0.52 m. The width and the height of the rectangular plane are 120 cm and 90 cm. The electric field magnitude was sampled 5 points in y-axis and 11 points in x-axis so we measured electric field magnitude in total of 55 positions on this plane. The probe is composed of a SMA connector and a metal rod shown in figure 3 (d). In figure 4, the reflection coefficient (S_{11}) of the probe was measured. As shown in figure 5, the horizontal- and vertical axes represent the position along the x- and y- axis, respectively. The electric-field strength is drawn in different color. From these contour maps of constant electric-field intensity, we observed that the field distribution in the position below 25 cm (the elevation angle within 0° to 25°) is within 1 dB variation. Besides the field distribution within 6 dB variation forms a rectangular footprint for this type of shaped-beam antenna.
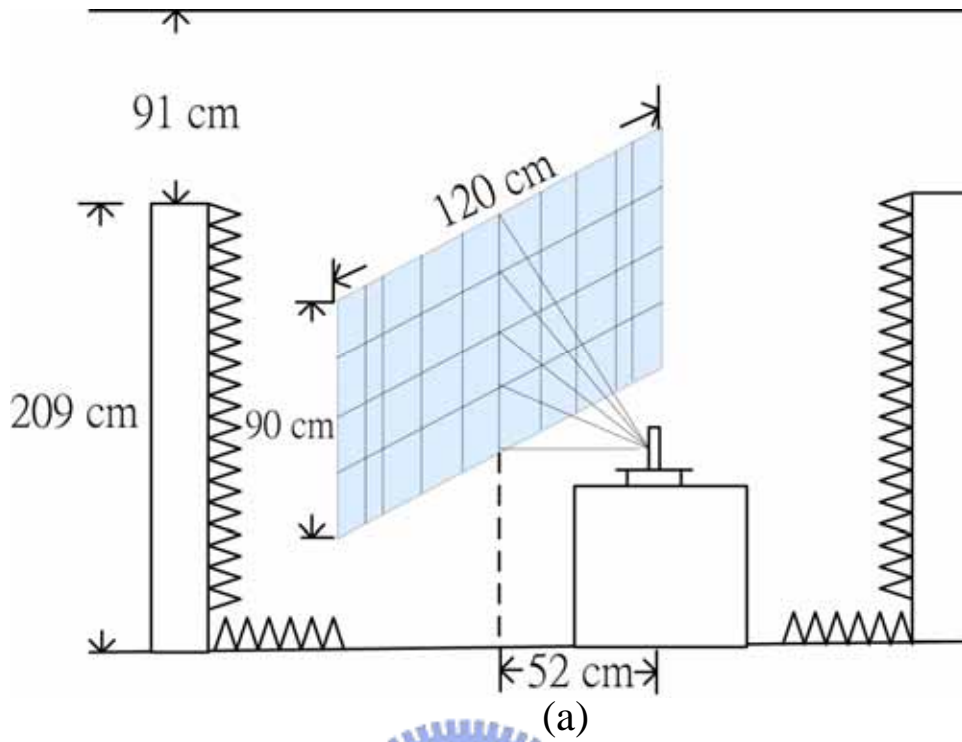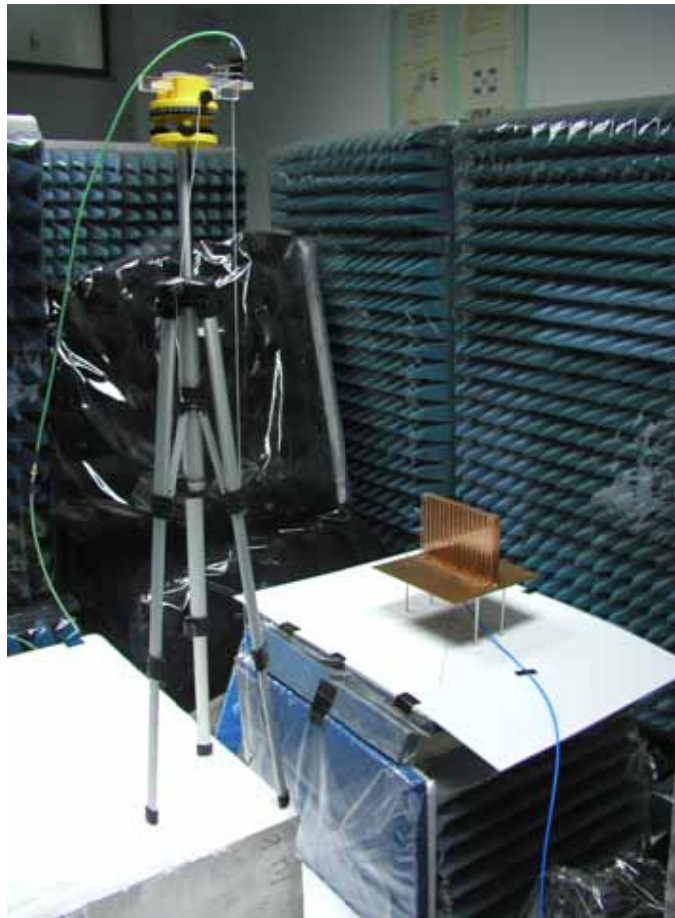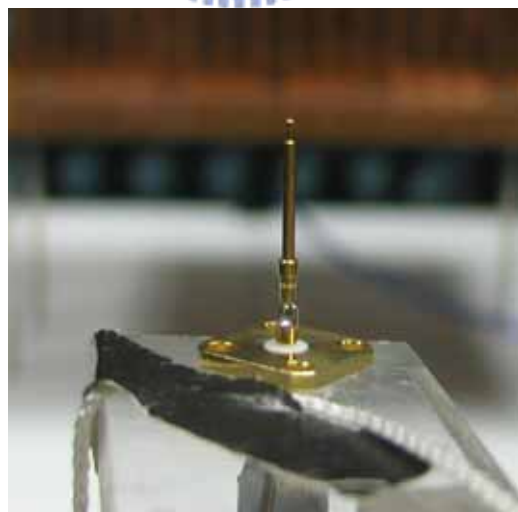
(a)

(b)

Figure 3: (a) Measurement setup in chamber (b) The probe is at the position $(x, y, z) = (0, 0, 52)$

(c)

(d)

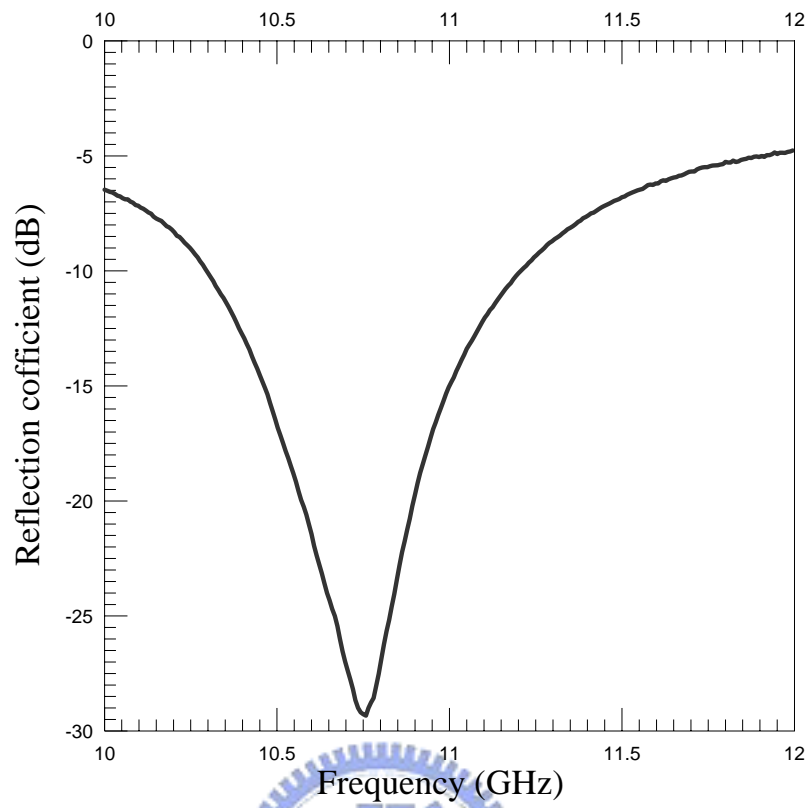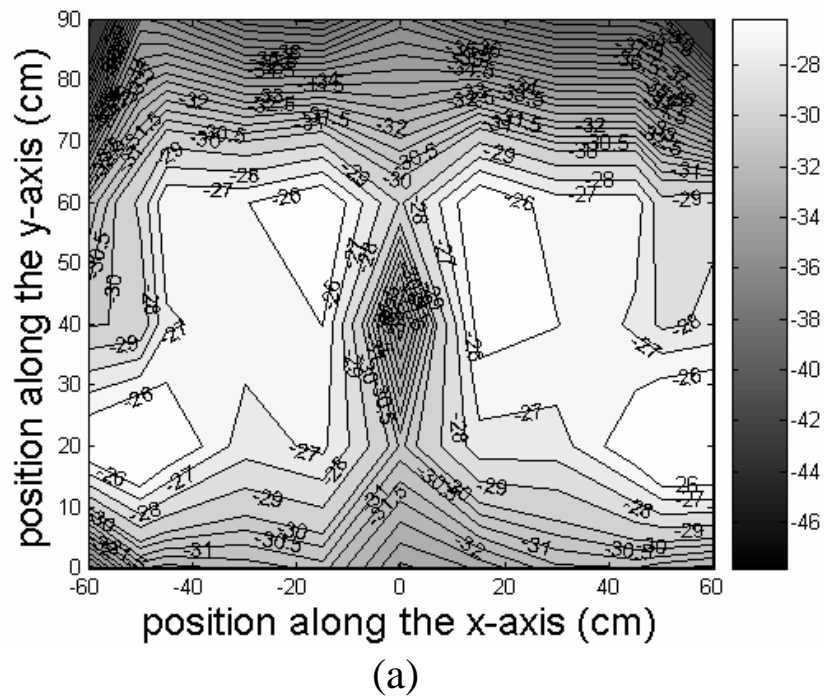Figure 3: (c) The probe is at the position $(x,\ y,\ z) = (0,\ 90,\ 52)$ (d) probe
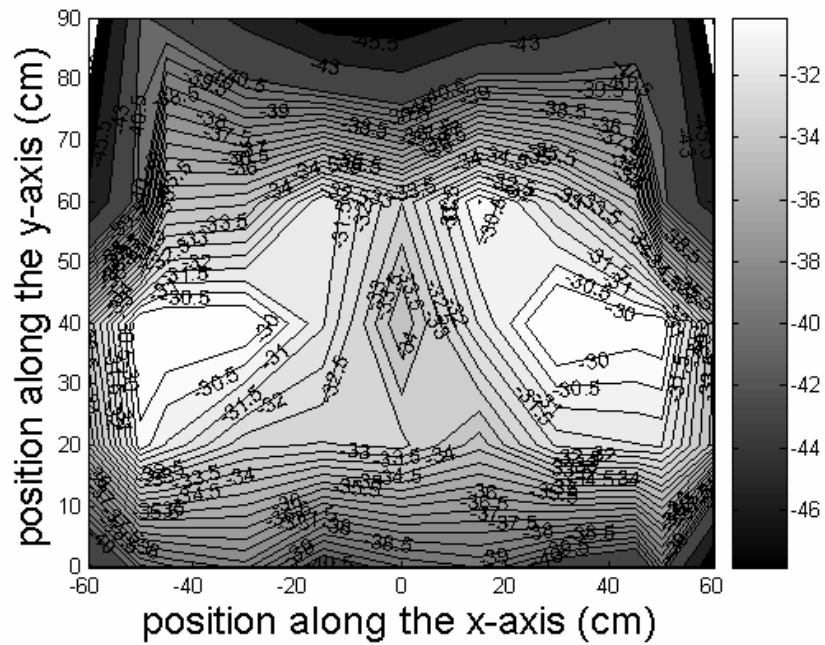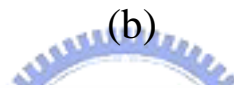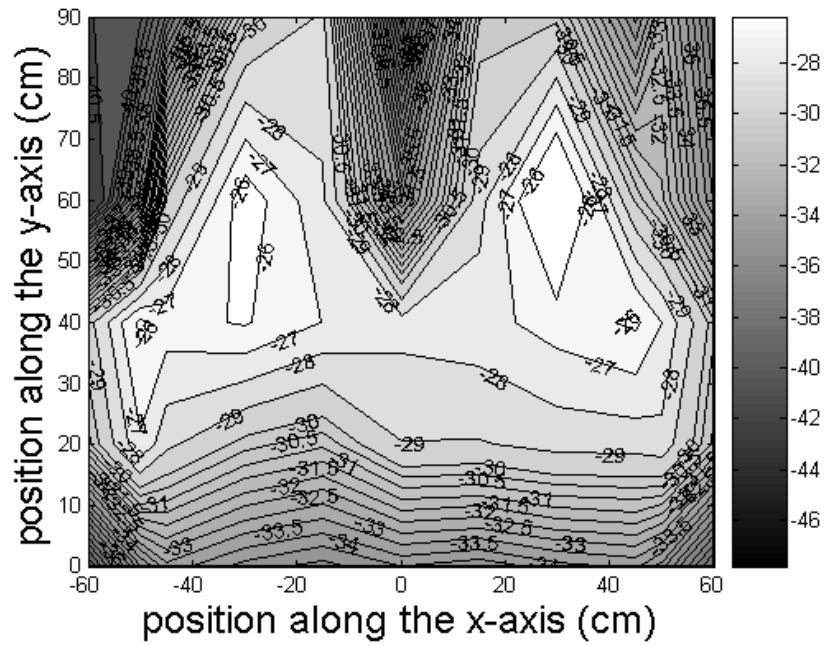
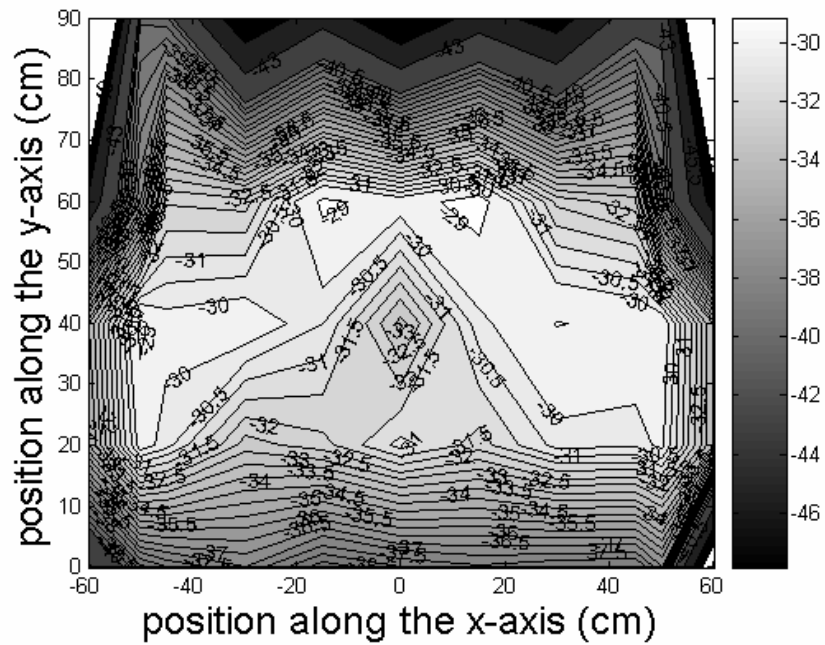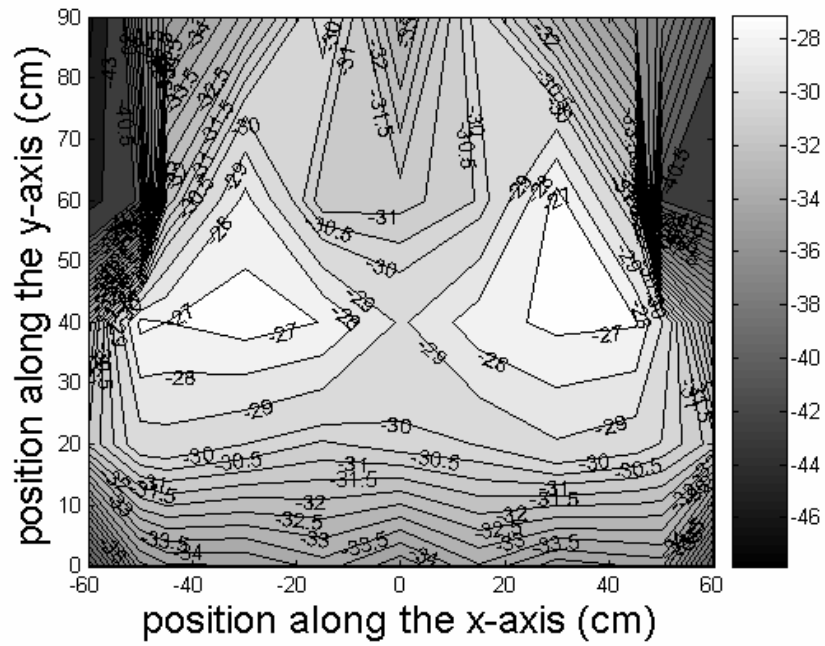Figure 4: Measured reflection coefficient for the probe.

(a)

Figure 5: Measured contour map of the y-direction electric field strength on a rectangular plane, (a) 10.90GHz.

(b)

(c)

Figure 5: Measured contour map of the y-direction electric field strength on a rectangular plane, (b) 11.37GHz, (c) 11.43GHz.

(d)

(e)

Figure 5: Measured contour map of the y-direction electric field strength on a rectangular plane, (d) 11.45GHz, (e) 11.47GHz.

(f)
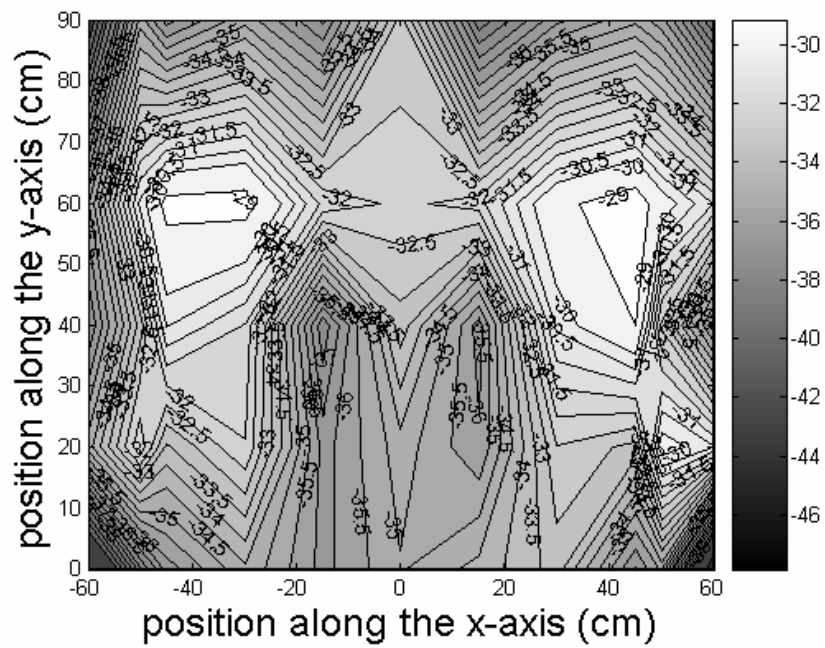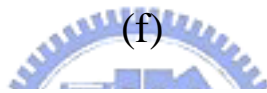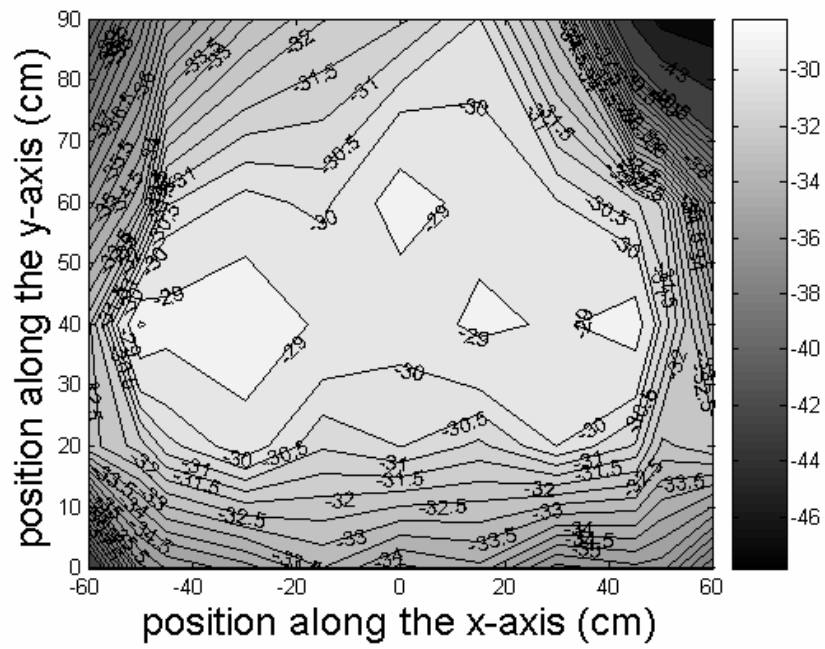

(g)

Figure 5: Measured contour map of the y-direction electric field strength on a rectangular plane, (f) 11.53 GHz, (g) 11.90GHz.
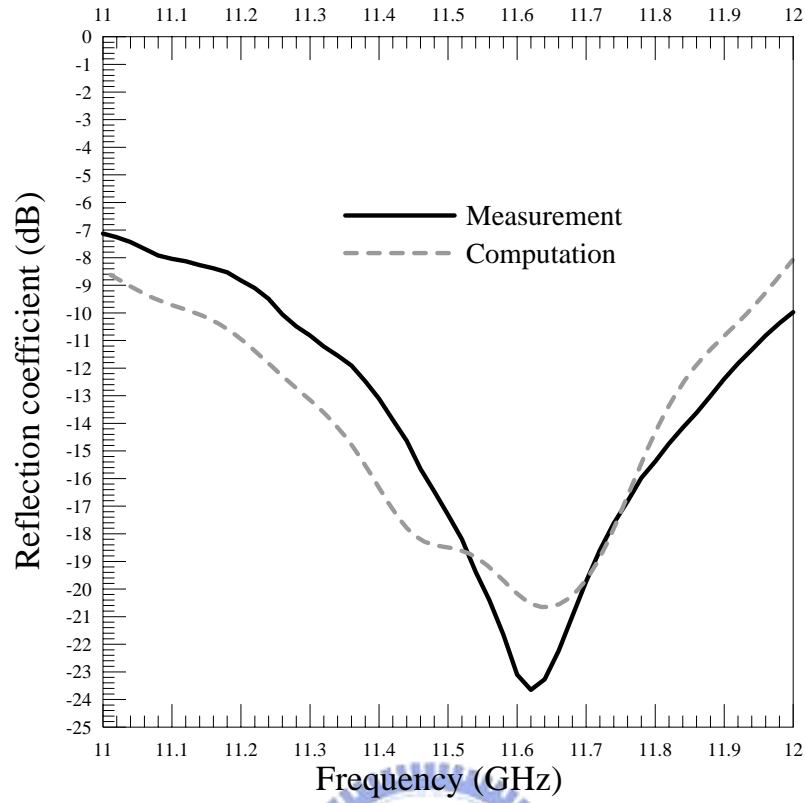
Figure 6: Measured and calculated reflection coefficient for the shaped-beam antenna

TABLE I

Measured radiation efficiency for the shaped-beam antenna

frequency GHz	Efficiency
11.30	75.54%
11.36	73.27%
11.42	72.58%
11.62	71.40%
11.80	70.70%

Figure 6 shows the measured and calculated reflection coefficient (S_{11}) for the planar

shaped-beam antenna.   The impedance bandwidth (S_{11} = -10dB) is around 740 MHz

(from 11.26 GHz to 12 GHz).   Notably, in the theoretical formulation, we assumed

that the current distribution along the excitation source is uniform. However, the non-uniform distribution of the current source may make some discrepancy between numerical and measured results.

Table 1 shows the radiation efficiency of this antenna operated from 11.30GHz to 11.80GHz. From the table, it is obviously to see that the efficiency is gradually decreasing. We may conclude that it is mainly due to the dielectric loss coming from the dielectric slab, which is used to support the metal strips. To reduce the dielectric loss, we may employ the low-loss microwave substrate when this antenna is operated in the millimeter wave region.

In the previous examples, a planar shaped-beam antenna was fabricated, and its radiation patterns at various different operation frequencies were measured. Besides, a computer program was developed to calculate the field distribution in the structure and the far-field radiation pattern, as well. The good agreement between the measured and calculated results was obtained. Therefore, we have a good position to carry out some further numerical simulations for inspecting the parameters affecting the radiation pattern. In the following section, we not only demonstrated the calculated radiation pattern, but also numerically discussed the variation of the radiation pattern against the changes in the following parameters (sensitivity analysis), such as the metal strip width, the relative dielectric constant, thickness of the dielectric layer, number of metal strips, and the location of the excitation source. Notably, in the following examples, the radiation pattern of the planar shaped-beam antenna has been normalized to that of the line source. Moreover, since the structure is closed in the backward and sideward directions, their radiation is inconsiderably in those directions. We only demonstrated the forward radiation pattern for the following examples.

2.3.2 Effect of the dielectric slab thickness on the radiation pattern

In Figure 7, we changed the thickness of the dielectric substrate to see the variation on the radiation pattern. In this example, the dielectric substrate with the relative dielectric constant εr=2.59 was used, and its thickness was varied from 0.9mm to 2.9mm. From this figure, it is apparently to see that the two radiation peaks gradually move from broadside- toward end-fire- direction. As we have mentioned earlier, the two radiation peaks are due to the leaky wave phenomenon. The peak radiation angle (counted from the x-axis) can be roughly determined by the formula given below [8]

$$\phi = \cos^{-1}(\beta_x / k_o)$$ (14)

As the thickness of the dielectric layer is increasing, the average dielectric constant of the waveguide channel (the region between the metal grating and the metal plate) is increasing. Accordingly, the phase constant along the x direction is increasing, therefore, the radiation angle moves toward low-grazing angles. Moreover, as shown in this figure, the leaky-wave phenomenon gradually disappears as the dielectric layer thickness increases to 2.5mm. We may conjecture that the thick dielectric layer causes the electromagnetic wave tend to be bound in the waveguide channel. In addition, this figure also reveals that, excluding the thick thickness cases, the shaped-beam pattern is not sensitive to the variation of dielectric thickness.
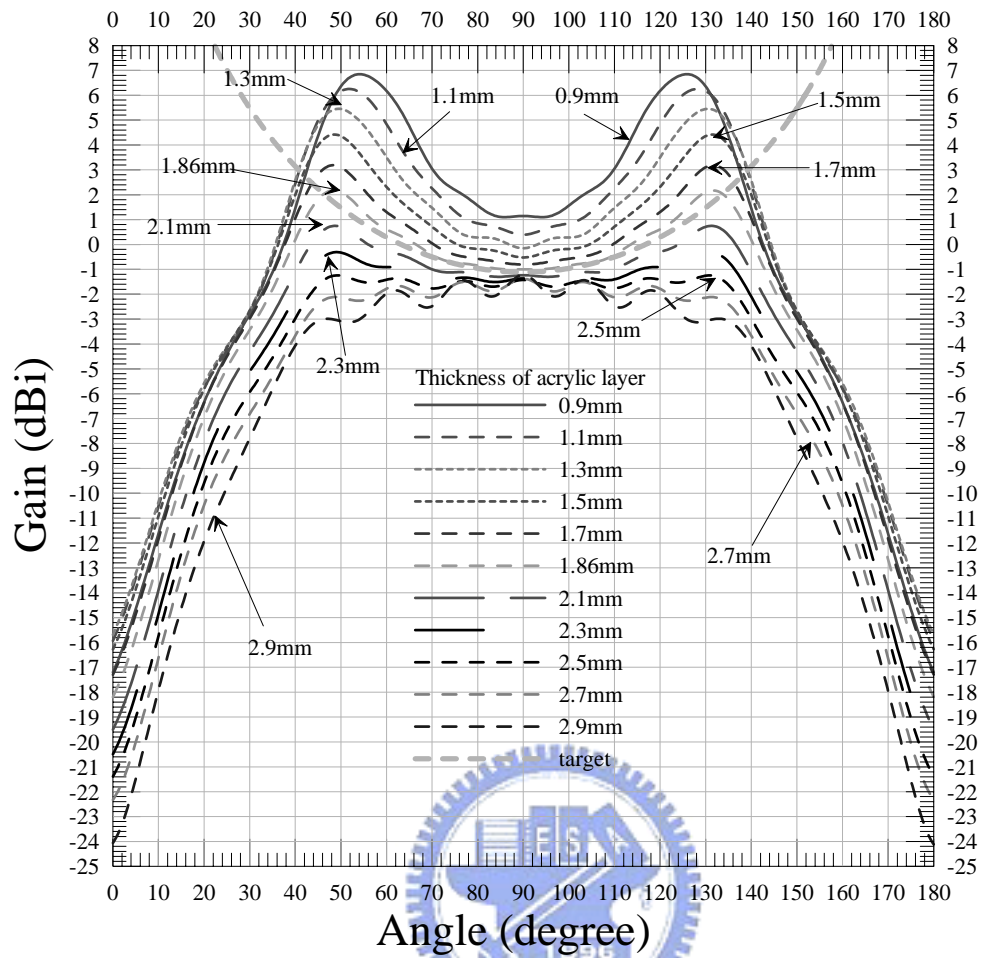
Figure 7: Radiation pattern for different dielectric layer thicknesses
at 11.43GHz (ε_r =2.59, a=5mm, b=15mm, t_m=0.05mm,
d_1=12.52mm, d_2=3.0mm)

2.3.3 Effect of the relative dielectric constant on the radiation pattern

In figure 8, we fixed the thickness of the dielectric layer and changed the relative dielectric constant from 1.9 to 3.3 to see the variation on the far-field pattern. Different from the previous case, the peak radiation angles almost remain as the relative dielectric constant increases.   It is instructive to know that the increase in the relative dielectric constant seems not to change the phase constant β_x.   For the high relative dielectric constant cases, the waves excited by the line source may be trapped in the waveguide channel and have a small attenuation (leaky) constant.   Besides, from this figure, we observe that there are some fluctuations with the radiation pattern; particularly for the cases with relatively high dielectric constant.   They are caused by the multiple reflections of the space wave, radiating directly from the line source, interacting with the dielectric layer having high dielectric constant.
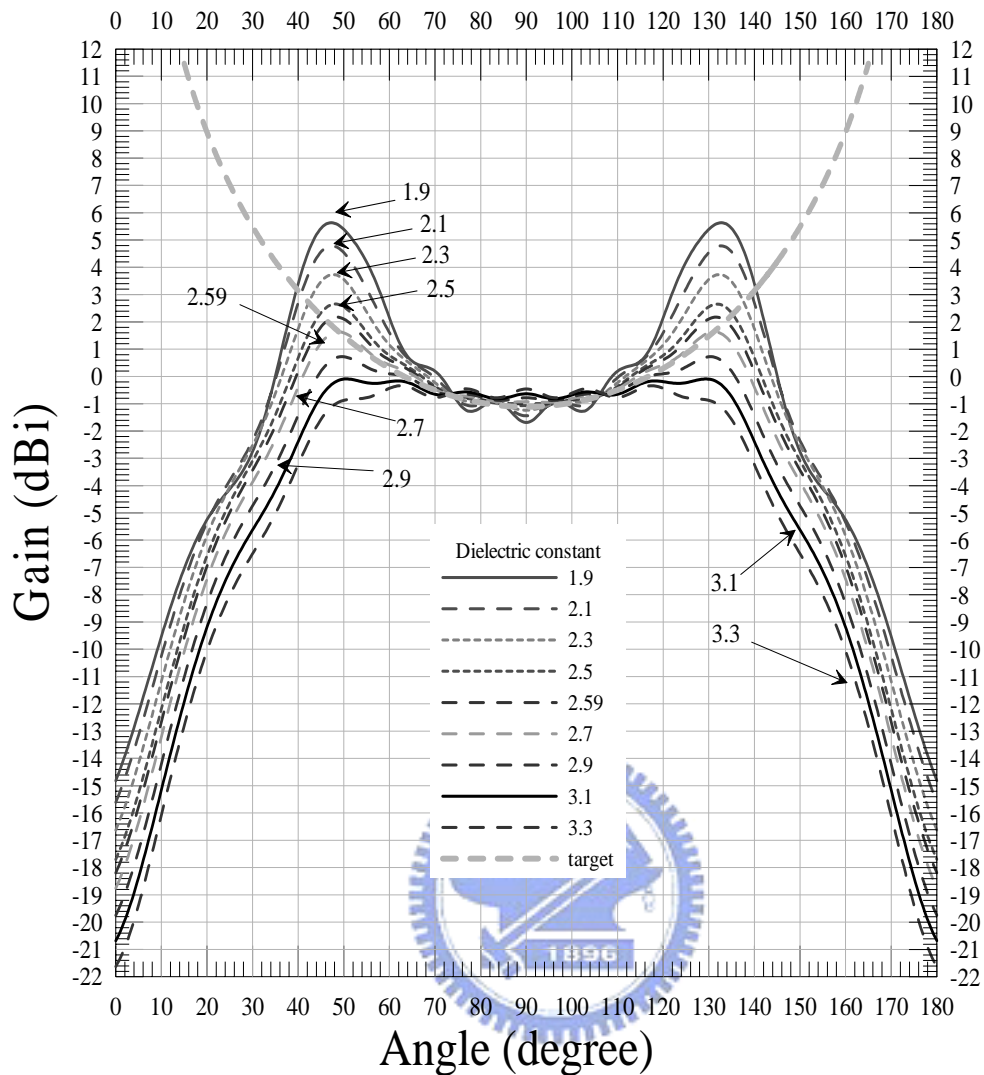
Figure 8: Radiation pattern for different dielectric constants at 11.43GHz.
(a=5mm, b=15mm, t_m=0.05mm, t_d=1.86mm, d_1=12.52mm, d_2=3mm)

2.3.4 Effect of the number of metal strips on the radiation pattern

In this example, we change the number of metal strips to see the variation on the radiation far-field pattern.   As demonstrated in figure 9, the radiation peak angle and strength, contributed by the leaky waves, are almost the same for the cases with 16, 24, and 32 metal strips.   It is because that the phase constant along the x direction almost remains the same value as the number of periods is large enough (greater than 16 in this case).
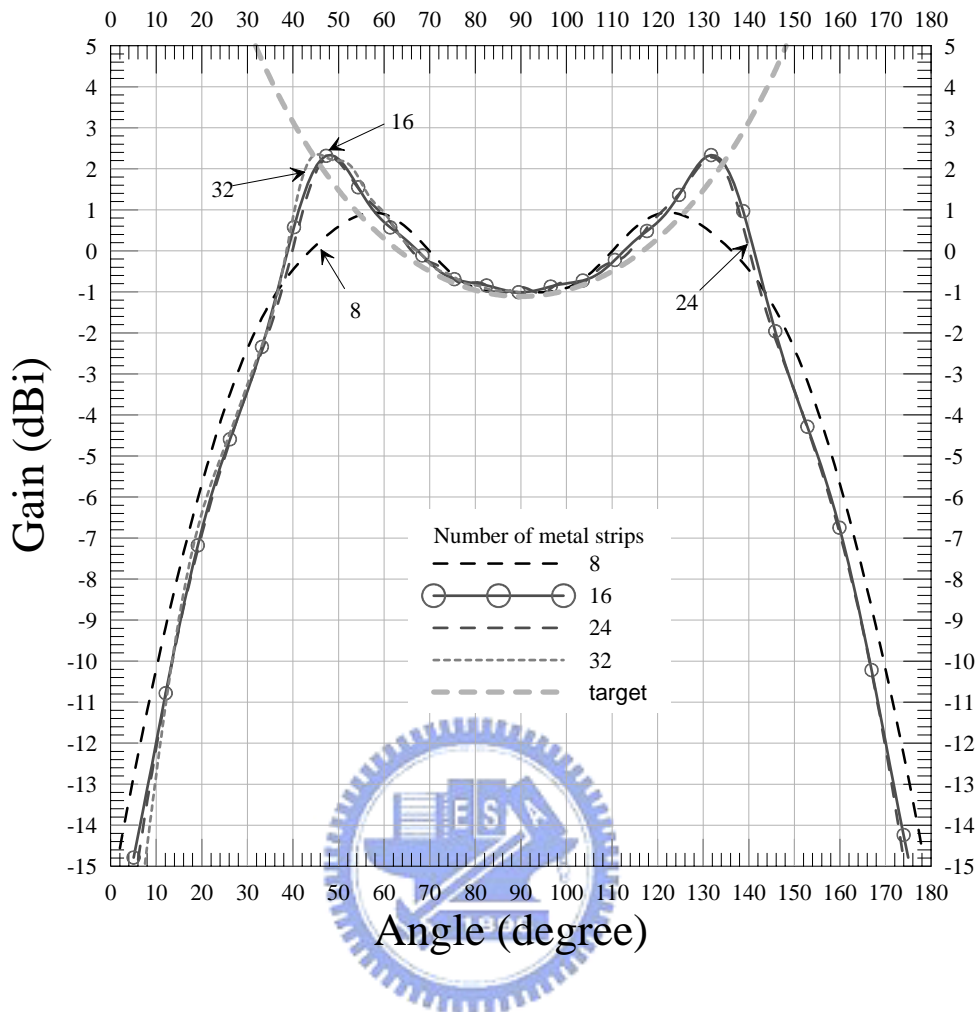
Figure 9: Radiation pattern for different number of metal-strip array (ε_r =2.59, a=5mm, b=15mm, t_m=0.05mm, t_d=1.86mm, d_1=12.52mm, d_2=3mm)

2.3.5 Effect of the line source position on the radiation pattern

In figure 10, we changed the position of the line source along the z direction to observe the variation on the far-field radiation pattern.   From the previous examples, we know that the function of line source is to excite the waveguide mode propagating along the ±x direction.   The propagating waveguide mode leaks its power into the surrounding medium.   Since the offset of the position of line source only affect the strength of excited waveguide mode, shown in equation (A17), the leaky wave angles (two radiation peaks) shall be unchanged.   On the other hand, the radiation intensity

in the forward direction (around 90 degree) changes since it is mainly contributed by the space wave radiation directly from the line source. Thus, we may observe that the field strength is decreasing as the line source is moving toward the metal plate. It may be explained by the image theory; that is, the image line source is directed opposite to that of the line source, reducing the strength in the far field. However, according to the curves shown in this figure, the position of line source can offer us a much greater degree of flexibility in tuning the beam shape to meet the target pattern.
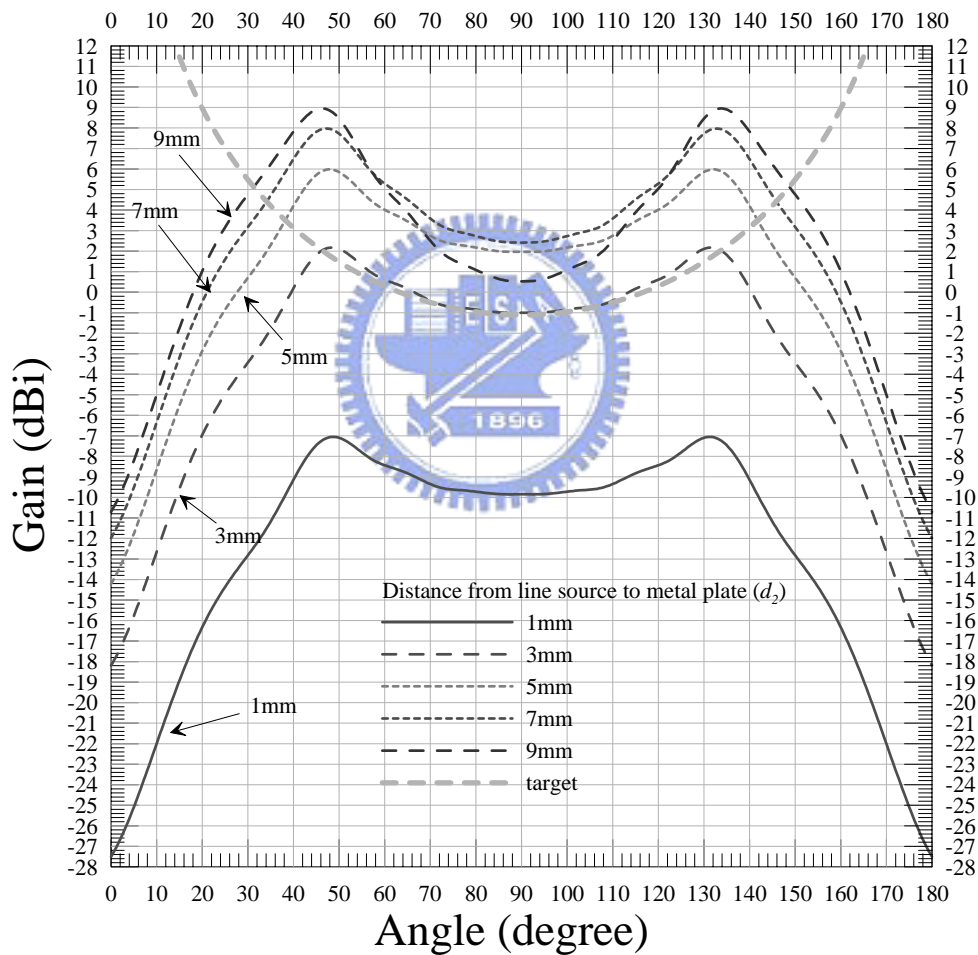
Figure 10: Radiation pattern for different distances from the line source to metal ground plane (ε_r =2.59, a=5mm, b=15mm, t_m=0.05mm, t_d=1.86mm , d_1=12.52mm, 11.43GHz)

2.3.6 Frequency range of operation

In the previous examples, we have investigated some parameters affecting the radiation far-field pattern. These results reveal that this antenna has considerable tolerance in the structure parameters and dielectric constant of the dielectric slab while maintaining the desired pattern. In the following example, we scanned the operation frequency from 10.9GHz to 11.93GHz to observe the variation on the radiation pattern. In doing so, the bandwidth for obtaining the desired $\sec^2$ pattern could be realized. From figure 11, we observed that the maximum deviation from the target pattern (angle ranges from 50° to 130°) is within 1dB for the frequencies ranging from 11.43GHz to 11.93GHz (500MHz bandwidth). Besides, it is apparently to observe that the maximum coverage angle shrinks in the lower frequency range from 10.9GHz to 11.35GHz.
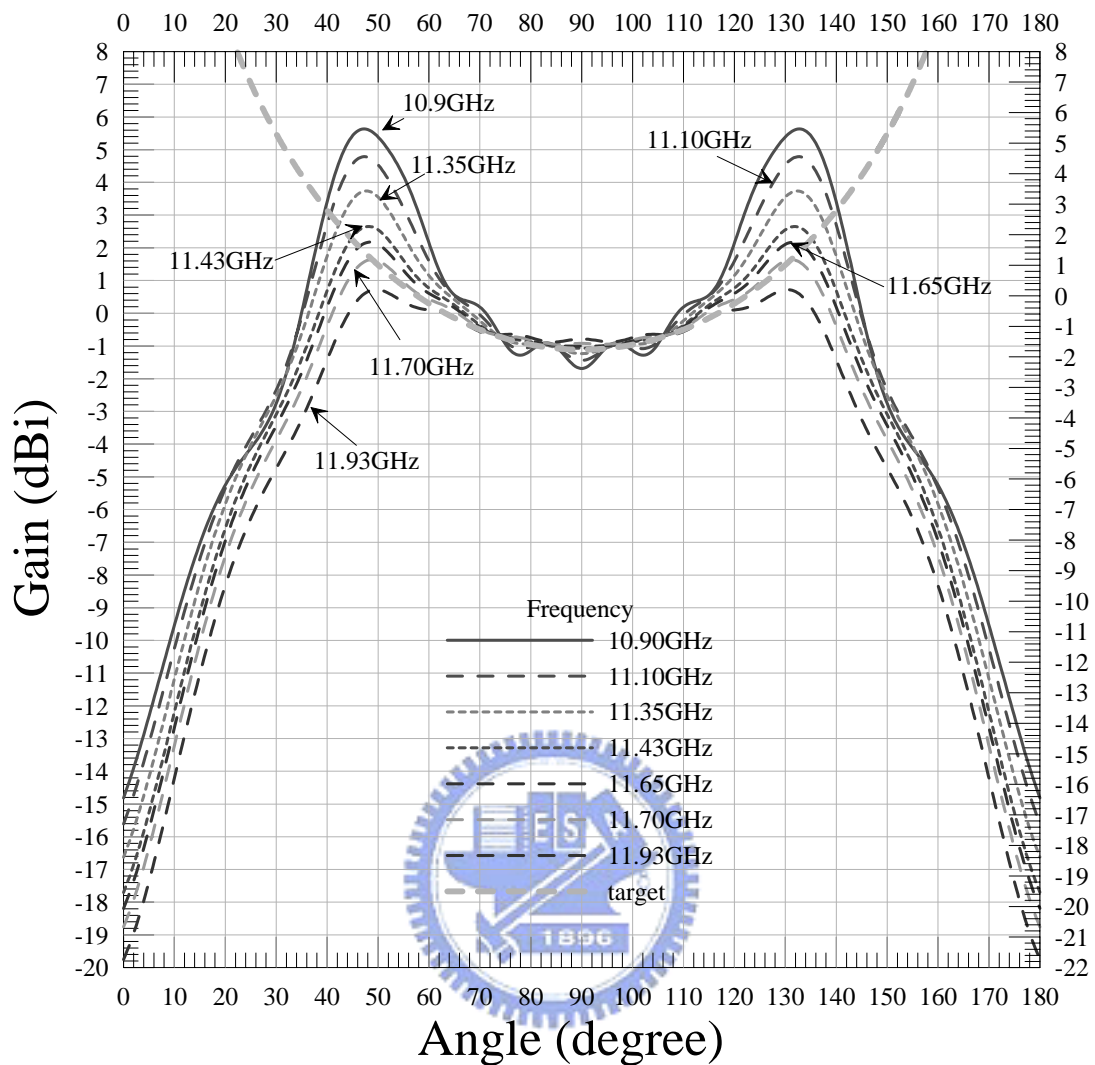
Figure 11: Radiation pattern for various frequencies (ε_r =2.59, a=5mm, b=15mm, t_m=0.05mm, t_d=1.86mm , d_1=12.52mm, d_2=3mm)

## 2.3.7 Shaped-bean antenna for wireless LAN band operation

In the previous examples and experimental results, a planar shaped-beam antenna was fabricated, and each antenna specification was measured in the frequency from 10.90GHz to 11.90GHz. In addition, each parameter affecting the radiation pattern was investigated. Because the antenna size is proportion to the operation wavelength, we can easily scale the structure parameters to any operation frequency range. We find another structure parameter set for the antenna operating at 2.4GHz and 5.2GHz,

and the size of new designs are more practical.   Firstly, the structure parameters were scaled to 2.4GHz and 5.2GHz. Then, we reduced the number of metal strips and adjust other structure parameters to maintain $\sec^2$ radiation pattern.   In addition, the pervious examples could provide us a design guide for tuning radiation pattern of the shaped-beam antenna.   From figure 12 and figure 13, we observed that the maximum deviation from the target pattern (angle ranges from 50° to 130°) is within 1dB.   As the number of the metal strip increases in both cases, the deviation from the target pattern is decreases.   The structure parameters for these antennas are listed in table 2.
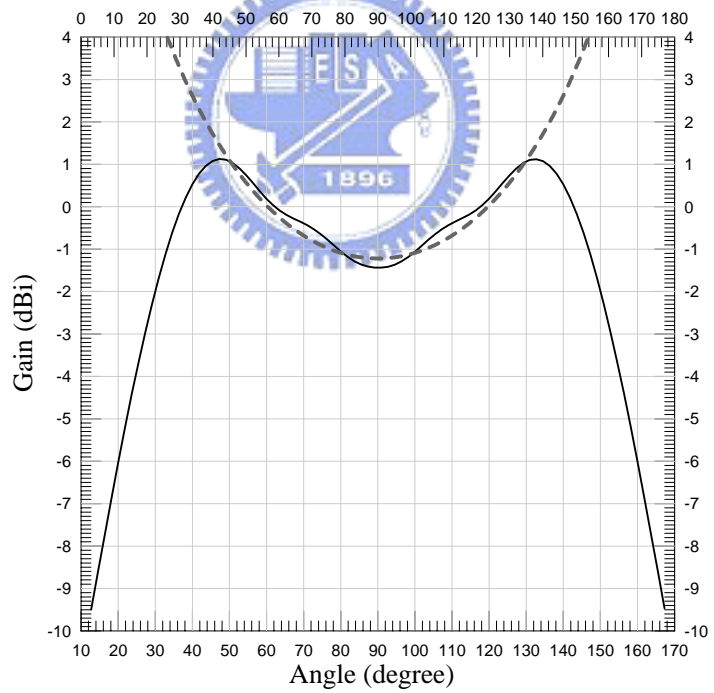
TABLE II

Structure parameters for shaped-beam antenna operating at 2.4 GHz and 5.2 GHz

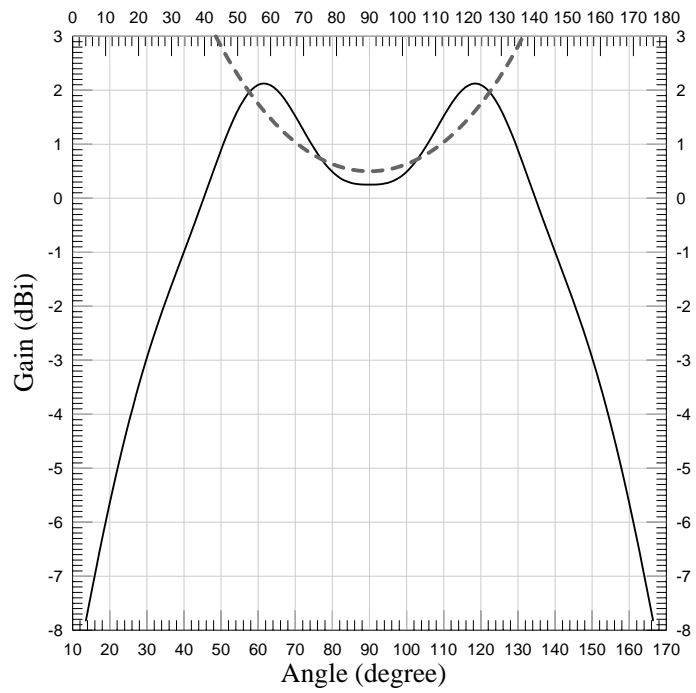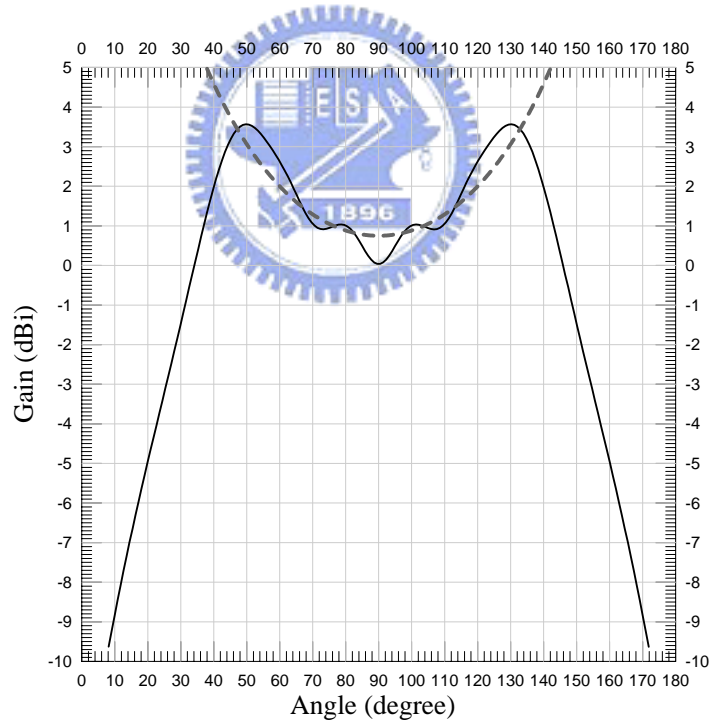| Operation Frequency	2.4 GHz		5.2 GHz	
antenna width	380 mm	238 mm	350 mm	241 mm
metal strip number	6	4	12	8
a	23.8 mm	23.8 mm	10.0 mm	11.0 mm
b	71.4 mm	71.4 mm	31.0 mm	33.0 mm
t_d	9.5 mm	9.5 mm	5.0 mm	5.0 mm
d_1	59.5 mm	59.5 mm	22.0 mm	22.0 mm
d_2	14.3 mm	14.3 mm	6.0 mm	6.0 mm
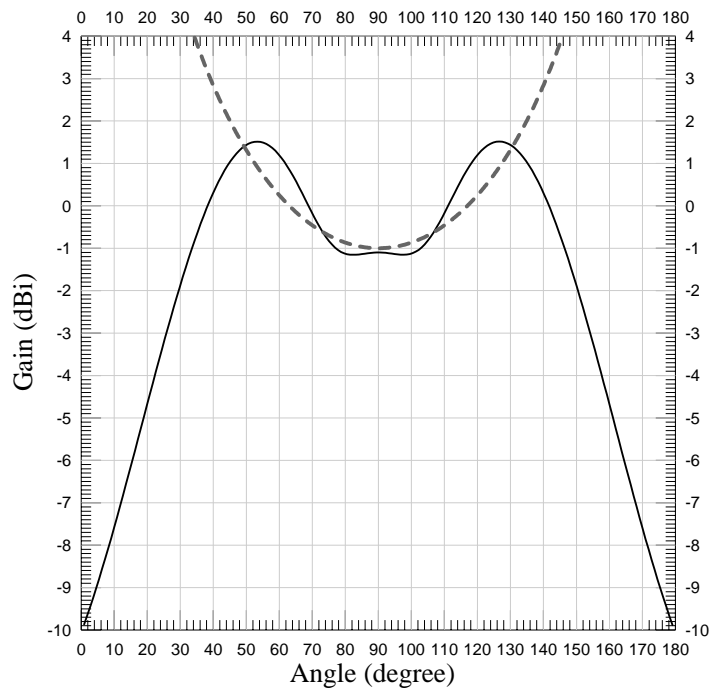
Figure 12: Radiation pattern for 2.4GHz, (a) 4 metal strips, (b) 6 metal strips.

Figure 13: Radiation pattern for 5.2GHz, (a) 8 metal strips, (b) 12 metal strips.